New model of pressure drop for the foam trays with dynamic bubbling process analysis

Peng Yan[a] | Hong Li[a] | Xingang Li[a,b] | Xin Gao[a,b,*]

[a] *School of Chemical Engineering and Technology, Tianjin University, National Engineering Research Center of Distillation Technology, Collaborative Innovation Center of Chemical Science and Engineering (Tianjin), Tianjin 300072, China*

[b] *Haihe Laboratory of Sustainable Chemical Transformations, Tianjin 300192, China*

* Corresponding author's Email, gaoxin@tju.edu.cn (X. Gao)

Abstract

Open-cell foams as the column tray are promising candidates for the purpose of process intensification in the distillation process. In this paper, the real foam porous structure is obtained based on Micro Computed Tomography (μ-CT), and the bubble formation process on pore-scale foam tray is discussed based on the VOF-CSF model (volume of fluid method-continuous surface force). The results show that the wettability (CA), superficial gas velocity (U_g), porous structure, and clear liquid layer height (H_{CL}) all affect a crucial factor of the foam tray - the liquid holdup in the porous channels (LHPC). It determines the effective porosity, which in turn affects the bubbling frequency and pressure drop. Meanwhile, the evolutionary mechanism of instantaneous pressure drop is analyzed based on the flow patterns, force analysis and interfacial phenomena. Moreover, the new model to predict pressure drop is proposed based on LHPC, which shows good consistency with experiments.

Keywords: foam tray, pressure drop, static contact angle, porous structure

1. Introduction

Porous foam materials have attracted more and more attention [1-5] due to their low density, high porosity, high specific surface area, good corrosion resistance, and strong support. Especially, it has the advantages of reduced pressure drop per unit height and large gas-liquid contact area, making it also a potential column internal structure. Such as foam corrugated structured packing [6-9], foam catalytical packing carrier [10-13], foam column tray [4,5,14-16], etc., have been proven to be more efficient than traditional column internals and are widely used in the chemical industry [4,5,14]. As one of the main applications, foam trays, although they have low-pressure drop and high mass transfer efficiency compared to the traditional column trays[4,5], there are still undesirable phenomena such as abnormal high-pressure drops[15], liquid weeping[16], and uneven gas distribution[17]. Therefore, in-depth research on the gas-liquid distribution inside the real foam pores, bubble evolution, and transient pressure drop is of great significance for the further development of the industrial application of the foam tray.

In recent years, many researchers have investigated the hydrodynamics and flow mechanism of the foam column tray. We all know that traditional metal and SiC foam structures are hydrophilic media, and the liquid phase can easily penetrate into the pores to form different forms of gas-liquid distribution [18]. Li et al. explored the gas distribution mechanism on the hydrophilic SiC foam tray, it was found that the foam structure and thickness have a significant impact on the pressure drop[15]. In addition, the SiC foam tray will cause abnormally high pressure due to weeping, which makes it difficult for the submerged foam orifice to form the first bubbling point. A large number

of studies have shown that the wettability of the porous media surface is closely related to the gas-liquid flow pattern in the pores [19] and found that changing the traditional tray from hydrophilic to hydrophobic can effectively reduce the pressure drop [20]. Therefore, modifying the SiC foam tray from hydrophilic to hydrophobic, Yan et al. found that the hydrophobic SiC foam tray also effectively reduced the pressure drop, and proposed the contact angle induced pressure drop [16] and the contact angle hysteresis effect [17] through the overall pressure drop decomposition. In general, these research results point out that the complex foam pore structure, gas-liquid flow pattern inside the porous channels, foam pore wettability, bubbling form, and other factors have varying degrees of influence on the pressure drop of the foam tray. However, current research methods, such as CT, high-speed imaging, and pressure drop measurement, are limited to the objective estimation of experimental results, and cannot deeply explore the interrelationship between the liquid-solid interaction, gas-liquid distribution, bubble shape evolution, and pressure drop of the foam tray. Thus the further development and application of the foam tray is limited. Therefore, this paper aims to research the bubble growth, gas-liquid distribution inside the transient foam tray, and the pressure drop based on CFD and provide valuable references for its further development.

Because the foam porous structure is one of the important factors for the reliability of CFD simulation results. However, many recent studies have approximated the foam structure to the accumulation of tetrakaidecahedron [9,21-24] or similar struts [25-29] to simplify the calculation, and lack a reliable prediction of the actual flow inside the porous channel. With the improvement of image reconstruction technology [30-33] and

computational fluid dynamics[27,34,35], the research for internal flow laws in porous channels can be better realized. However, due to the complexity of the foam structure, it is difficult to construct an ideal grid through structural grids, or it may lead to a large number of grids and low computational efficiency due to ensuring the authenticity of the grids as much as possible. As a result, the current researches based on the combination of CT reconstruction and CFD are mostly limited to steady-state research on homogeneous heat transfer [35,36], pressure drop [37,38], and flow distribution [32,34,39-42]. A few researchers apply it to research the heterogeneous gas-liquid distribution due to the time-consuming calculation, and Li et al. only scans and reconstructs the two-dimensional foam structure plane to study the bubble evolution mechanism[43]. Therefore, based on the real three-dimensional foam structure to transiently study the bubble mechanism of the foam tray is faced with the following problems: 1. Ideal mesh is difficult to construct, 2. The number of meshes is huge, 3. The calculation of the internal gas-liquid two-phase is easy to diverge and time-consuming.

Therefore, this paper aims to solve the above problems. Firstly, reconstructing the real structure of the SiC porous channel based on Micro Computed Tomography (μ-CT) and using the real pore structure as the foam column tray (in Section. 2). Secondly, the numerical simulation of bubbling growth on different wettability foam tray is realized by adding the volume force source term to the momentum equation (in Section. 3). Thirdly, the real foam characteristic structure is constructed through the hybrid mesh of polyhedron and hexahedron, and the number of meshes is reduced on the basis of ensuring the authenticity of the foam structure. To balance the reliability and efficiency

of the calculation results, local mesh refinement encryption is used in the bubble rising path (in Section. 4.1). Fourthly, the dynamic bubbling process was investigated with multiple factors, such as superficial gas velocity (0.1 m/s < U_g < 1.0 m/s), static contact angle (45^o < CA < 135^o), porous structure (1.04 mm < D_C < 1.9 mm), and clear liquid layer height (30 mm < H_{CL} < 60 mm), and its influence on the gas-liquid distribution inside the foam pores, bubble growth, and pressure drop (in Section. 4.4 – 4.7). Finally, based on this research results, a new general equation for the pressure drop of foam tray was constructed to provide a reference for the further development and utilization of foam trays (in Section. 5).

2. Reconstruction of real structure for foam tray

Foam SiC trays were supplied by the Institute of Metal Research, Chinese Academy of Science[15]. The real structure of the SiC foam tray is shown in Figure 1a, b. The thickness of the experimental foam tray (4 mm - 12 mm) and the bubble size distribution (in the air-water system, the bubble size distribution is concentrated between 3 mm and 6 mm) are considered comprehensively. Finally, the foam block with L × W × H = 6 mm × 6 mm × 4 mm is selected as the representative foam cell, which not only saves computing resources, but also does not affect the actual situation of bubble formation. Using Avizo software to analyze and scan the structural pictures of different porous foam materials. Based on the difference in the gray value of the foam struts and porous channels, it is divided into the solid region and fluid region, and its boundary value is determined based on the real structure porosity, thereby ensuring the authenticity of the foam structure.

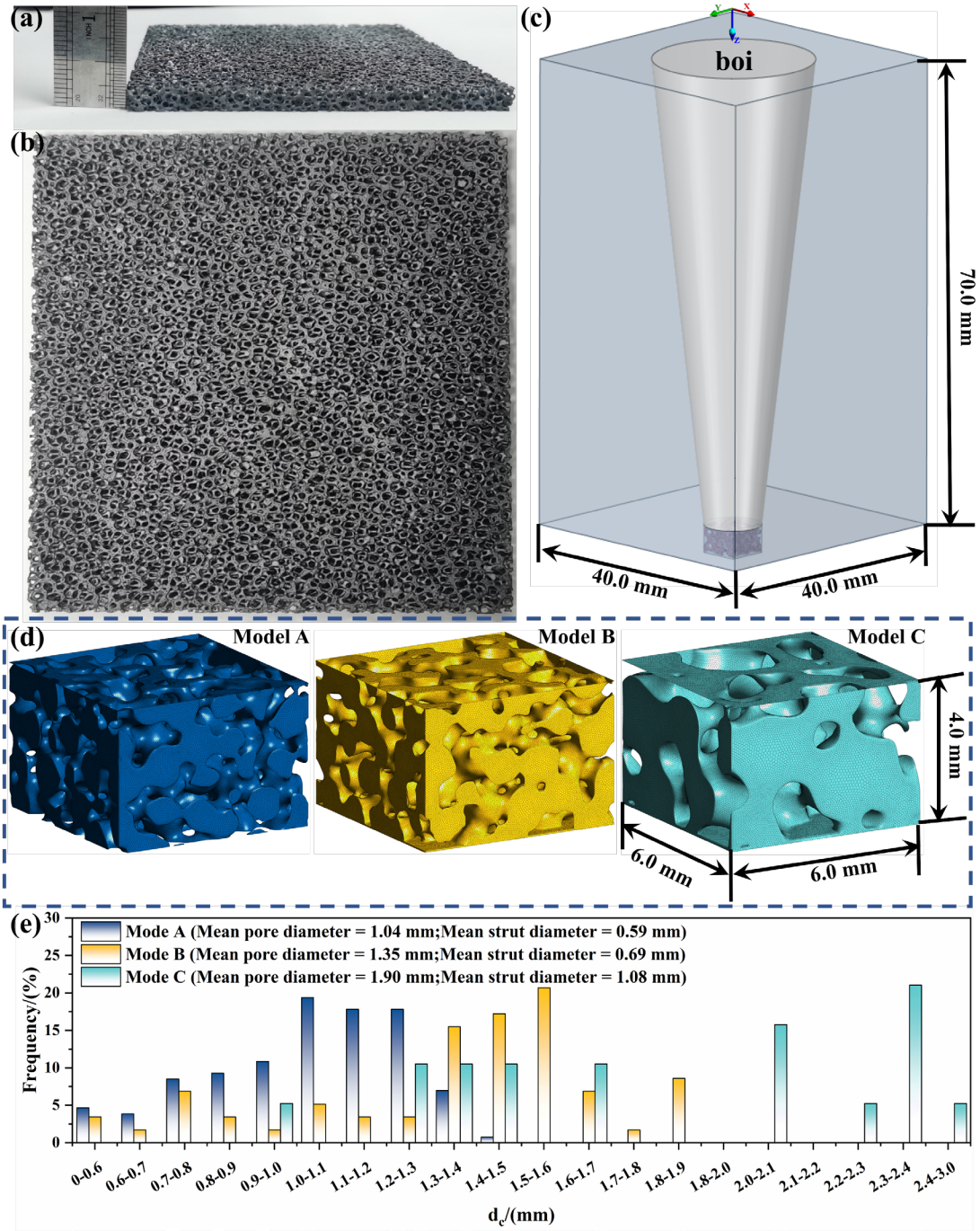

FIGURE 1 Images of SiC foam tray investigated: (a) top view and (b) front view; (c) geometric model; (d) 3D reconstruction of the real foam structure; (e) The pore size distribution of the SiC foam monolithic tray acquired by x-ray 3D imaging techniques.

In this paper, three foam SiC materials with different pore diameter were selected to study the effect of the pore structures on the bubbling process and the pressure drop. The porosity of the initial foam block is controlled at 60% by adjusting the boundary

of the fluid-solid region, which is consistent with the real situation. Next, the reconstructed three-dimensional real foam structure is imported into SPACECLAIM to establish a fluid domain (in Figure 1c), the local mesh refinement domain (boi region in Figure 1c) is established through the trajectory of bubble motion. Then imported into FLUENT MESHING to refine and smooth the internal rough porous structure to make it more conducive to numerical calculations (in Figure 1d). Meanwhile, the porosity of the optimized models A, B and C are 60.6%, 61.5% and 58%, respectively. The pore size distributions of the three foam structures obtained by spheroid-like analysis of the foam unit cells are shown in Figure 1e. The mean pore sizes for models A, B, and C are 1.04 mm, 1.35 mm, and 1.90 mm, respectively. Using the same method for the solid region, the mean strut diameters for models A, B, and C are 0.59 mm, 0.69 mm, and 1.08 mm, respectively. Unreasonable optimization for the geometric structure will affect the reliability of the simulation results. Therefore, a combination of polyhedral mesh and hexahedral mesh was used to ensure the authenticity of the foam porous structure as much as possible. For a detailed discussion of this content, see Section 4.1 of Results and Discussion.

3. Mathematical modeling

Considering the clear gas-liquid phase separation inside the porous foam material and the capture of the bubble shape above the foam column tray, the volume of fluid (VOF) model is used to simulate the bubbling process. This research focuses on the pressure drop of the foam column tray and the liquid holdup in the porous channels (LHPC) with Ug < 1.0m/s. The laminar flow model is adopted, and some coarse-

grained mathematical models (RANS, LES, etc.) are not introduced to describe turbulent flow, thus the additional error caused by the disordered vortex structure under turbulent conditions is eliminated. Moreover, the method of transforming the N-S equation into a linear equation adopts the finite volume method. This paper adopts double precision and 10^{-3} as the iterative convergence judgment conditions to avoid errors in computer solutions as much as possible. The laminar flow and incompressible model are adopted by solving the continuity equation (Equation 1) and Navier Stokes equation (Equation 2) to understand the process in detail.

Continuity equation:

$$\frac{\partial}{\partial t}\left(\alpha_i \rho_i\right) + \nabla \cdot \left(\alpha_i \rho_i \mathbf{u}_i\right) = 0,\ i = g, l \tag{1}$$

Momentum conservation equation:

$$\frac{\partial}{\partial t}\left(\rho \mathbf{u}\right) + \nabla \cdot \left(\rho \mathbf{u}\mathbf{u}\right) = -\nabla P + \nabla \cdot \left(\mu\left(\nabla \mathbf{u} + \nabla \mathbf{u}^T\right)\right) + \mathbf{F}_{VOL} + \rho \mathbf{g} \tag{2}$$

The density and viscosity in the momentum equation and the continuity equation both use volume average density and volume average viscosity, as shown in Equations 3 and 4.

$$\rho = \alpha_g \rho_g + \alpha_l \rho_l \tag{3}$$

$$\mu = \alpha_g \mu_g + \alpha_l \mu_l \tag{4}$$

Whether in the porous channel or the bubbling region, surface tension, a vital role, is caused by the attraction between molecules in the fluid. At the gas-liquid surface, the net force is radially inward, and the combined effect of the radial component of the force on the entire spherical surface is to shrink the surface, thereby increasing the pressure on the concave side of the surface. In this paper, the continuous surface force

(CSF) model is used to interpret the surface tension as a continuous three-dimensional effect across the interface, rather than the boundary value condition on the interface. The surface tension effect is simulated by adding a source term to the momentum equation. That is, the forces normal to the interface can be expressed as the following equation.

$$\Delta p = \sigma\left(\frac{1}{R_g}+\frac{1}{R_l}\right) \tag{5}$$

where ΔP is the differential pressure between the two fluids on both sides of the interface, σ_{ij} is surface tension coefficient, R_g and R_l are surface curvature as measured by two radii in orthogonal directions. The surface curvature is computed from local gradients in the surface normal at the interface. The calculation expression of curvature k is shown in Equation 6.

$$\kappa = \nabla\cdot\hat{n} = \frac{1}{|\mathbf{n}|}\left[\left(\frac{\mathbf{n}}{|\mathbf{n}|}\cdot\nabla\right)|\mathbf{n}| - (\nabla\cdot\mathbf{n})\right] \tag{6}$$

The continuous surface force (CSF) [44] model used in this paper can estimate the effect of wall adhesion at the fluid interface in contact with the balanced rigid porous boundary based on the equilibrium contact angle (θ_{wall}) between the fluid and the porous channel wall.

$$\hat{n} = \mathbf{n}_{\mathbf{wall}}\cos\theta_{wall} + \mathbf{t}_{\mathbf{wall}}\sin\theta_{wall} \tag{7}$$

$$\mathbf{t}_{\mathbf{wall}} = \nabla\tilde{c}(\mathbf{x}) = \frac{\nabla\tilde{c}(\mathbf{x})}{\left|\nabla\tilde{c}(\mathbf{x})\right|} \tag{8}$$

where θ_{wall} is the contact angle at the porous wall, $\hat{n}$ is the surface normal at the cell next to the porous wall. $\mathbf{n}_{\mathbf{wall}}$ is the unit wall normal directed into the wall, $\mathbf{t}_{\mathbf{wall}}$ is computed using Equation 8 with the fluid color $\nabla\tilde{c}(\mathbf{x})$ reflected at the porous wall.

t_{wall} also is explained as a unit vector tangent to the porous wall. Therefore, the gas-liquid surface tension can be written in terms of the pressure jump across the surface, the force at the surface can be expressed as a volume force using the divergence theorem. It is this volume force (in Equation 9). that is the source term that is added to the momentum equation (in Equation 2).

$$F_{VOL} = \sigma_{ij} \frac{\rho \kappa_i \nabla \alpha_i}{\frac{1}{2}\left(\rho_i + \rho_j\right)} \tag{9}$$

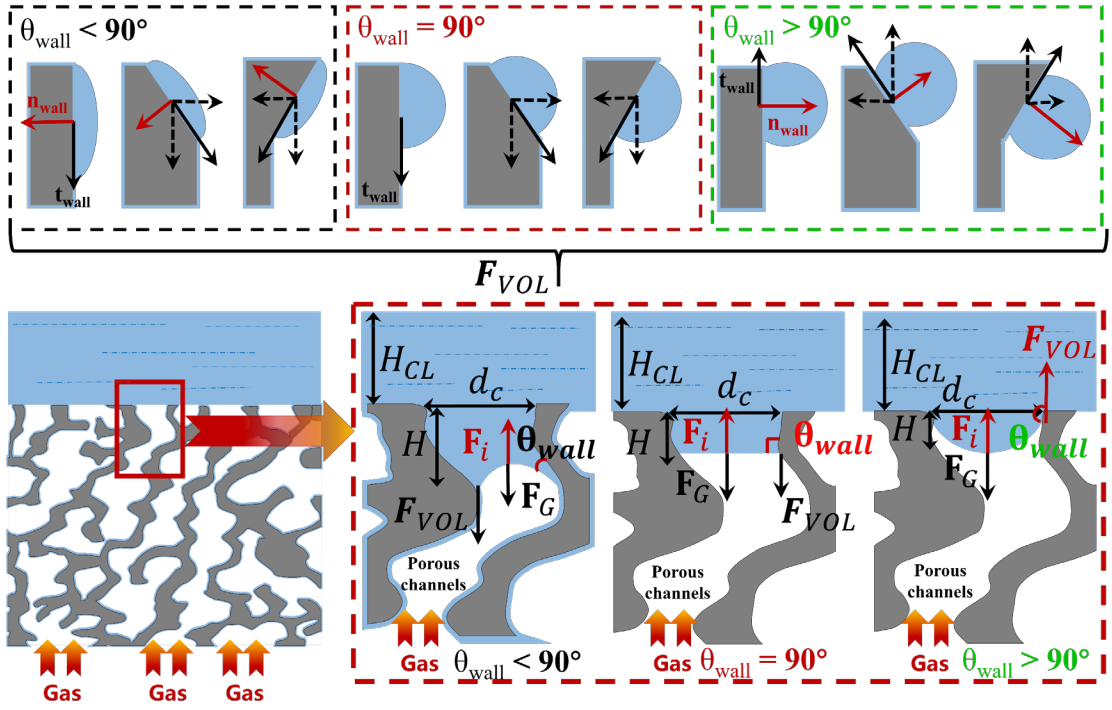

FIGURE 2 Force analysis in different wettability θ_{wall} < 90°, θ_{wall} =90° ,θ_{wall} > 90°, Where F_i , F_G and F_{VOL} are generated by gas impact force, liquid weight and volume force.

The different wettability of the porous media surface will seriously affect the whole operation process, so the different wetting states (static contact angle) of the porous media are analyzed. In Figure 2, when the CA (static contact angle) < 90°, the porous media wall in a wetting regime. The liquid attached to the porous wall tends to pull down along the porous wall, and there is a squeezing force perpendicular to the

porous wall. The liquid phase attached to the porous wall is subjected to a downward adhesive force component. When the CA = 90°, the squeezing force perpendicular to the wall disappears, but the liquid phase attached to the wall still suffers a downward adhesion component. When the CA > 90°, the porous media wall in a non-wetting regime, the liquid attached to the porous wall tends to accumulate into droplets inside. Therefore, the liquid attached to the porous wall will be subjected to a component force that shrinks upward along the porous wall. The direction perpendicular to the porous wall is subject to the component force directed to the inside of the liquid phase. When the liquid phase inside the pore reaches a dynamic equilibrium state, the inner liquid is also subjected to an upward gas phase driving force F_i and downward gravity F_G as shown in Equations 10 and 11.

$$F_i = \int_{A_c} \rho_g \cdot U_g{}^2 dA = \rho_g \cdot U_{g,m}{}^2 \cdot A_c \tag{10}$$

$$F_G = \rho_l \cdot g \cdot (H_{CL} + H) \cdot \mathrm{A_c} \tag{11}$$

where ρ_G and ρ_L are the density of gas and liquid respectively, U_g is the superficial gas velocity, A_c is the cross-sectional area of the channel, H is the height of the liquid in the porous channel, H_{CL} is the height of the clear liquid layer, g is the acceleration of gravity.

4. Results and discussion

4.1 Mesh independence verification

To analyze the errors caused by ignoring Taylor's higher-order terms in the numerical simulation process, mesh independence is done. Three mesh sizes are established as shown in Figure 3a. The difference in meshing is mainly concentrated in

the domain I (porous channel) and the domain II (boi: bubble trajectory).

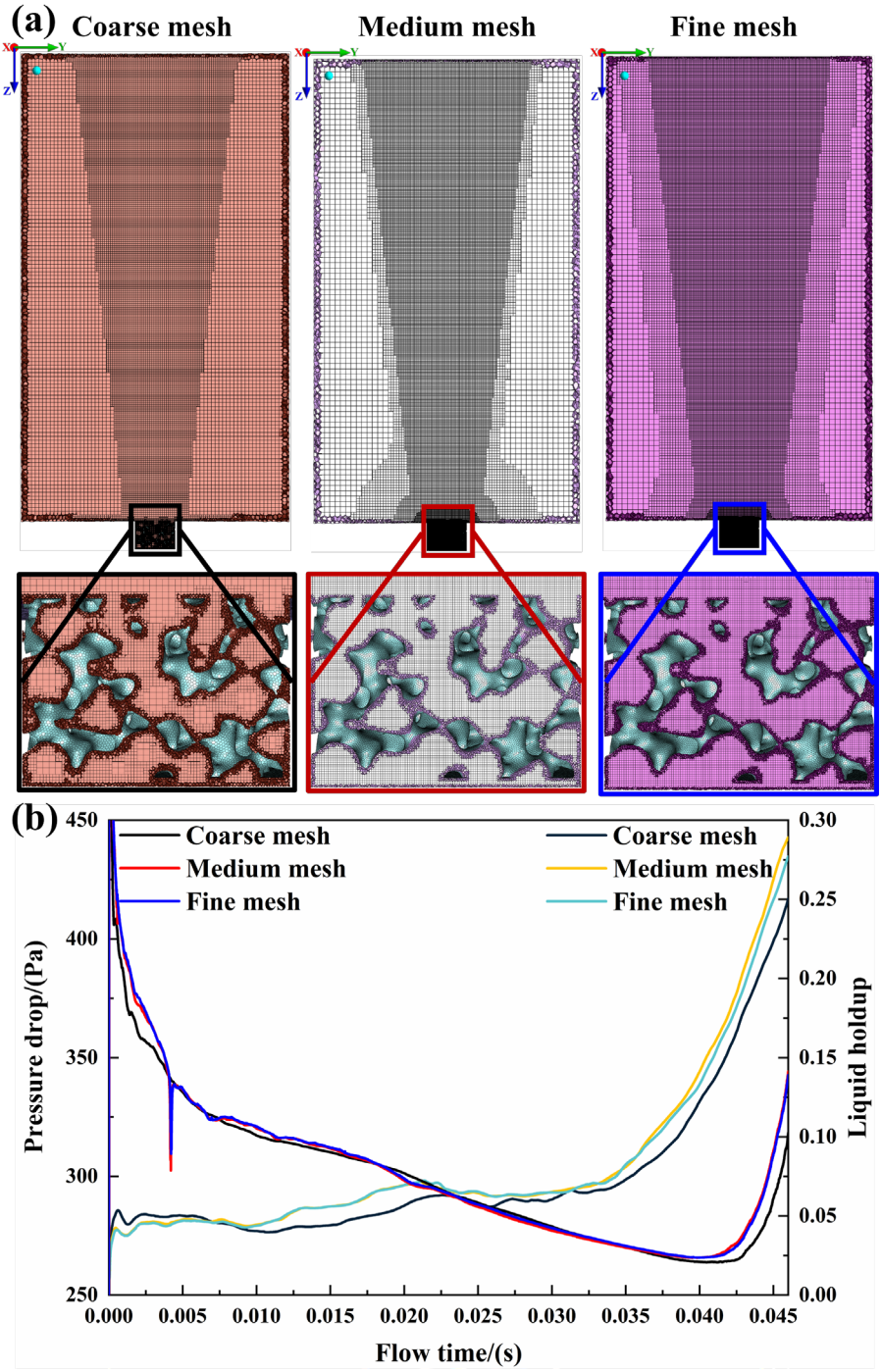

FIGURE 3 (a) Details of mesh generation: coarse mesh 1740578 maximum quality 0.77327459, Medium mesh 3998241 maximum quality 0.78954562, Fine mesh 4728259 maximum quality 0.78093014;(b) the comparison results of the pressure drop and the liquid holdup in the porous channel with different mesh number at U_g = 0.3 m/s and CA = 45°

Coarse mesh: The maximum mesh in Domain I is 0.07 mm with a growth rate of 1.05. The maximum mesh in Domain II is 0.4 mm with a growth rate of 1.2. Medium

mesh: The maximum mesh in Domain I is 0.06 mm with a growth rate of 1.05. The maximum mesh in Domain II is 0.2 mm with a growth rate of 1.2. Fine mesh: The maximum mesh in Domain I is 0.05 mm with a growth rate of 1.05. The maximum mesh in Domain II is 0.2 mm with a growth rate of 1.05. The simulation results with different mesh sizes show that there is a certain error between the calculation results of the coarse mesh and the medium mesh and fine mesh (in Figure 3b). But when the number of meshes increases from medium mesh to fine mesh the densification and refinement of the mesh has almost no effect on the simulation results of the LHPC and P_{total}. Therefore, in the case of rational use of computing resources, this paper adopts the meshing strategy of medium mesh to generate the computational fluid domain of the other foam structures, and this is the final mesh model.

4. 2 Model verification

Based on Model B, this paper simulates the dry pressure drop at different inlet velocities (U_g). Meanwhile, the wet pressure drop of Model B was simulated when CA=55° (hydrophilic foam tray) and H_{CL} = 0.03 m (clear liquid layer height). As shown in Figure 4a， the simulation results of dry pressure drop are compared with the improved Eugen's equation (in Equation 12) proposed by Bracconi[38]. The equation is derived from the double correction of the experimental and CFD simulation results. When the strut is a triangular column, A' and B' in the Equation 12 are 266 and 1.2 respectively.

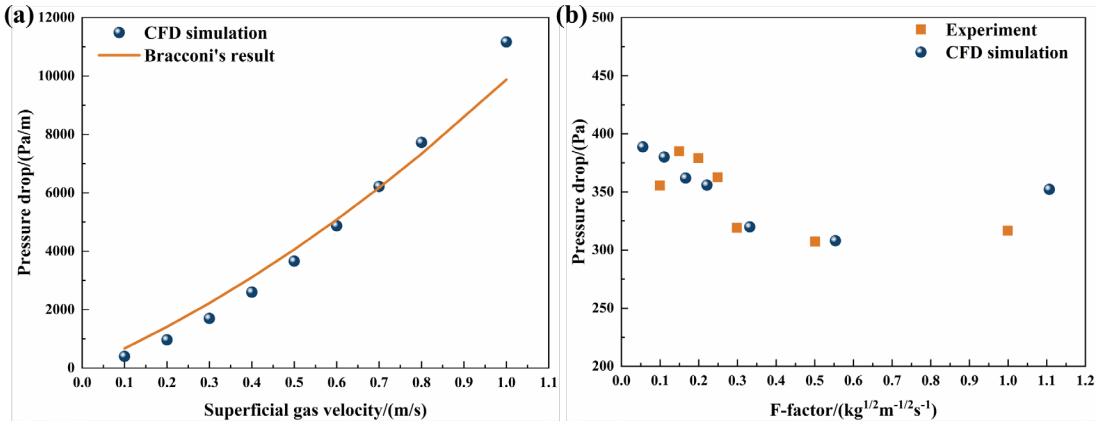

FIGURE 4 (a) the dry pressure drop[38]; (b) the wet pressure drop[15] (CA = 55°, H_{CL} = 0.03 m, Model B).

$$\frac{\Delta P}{L} = A' \frac{(1-\varepsilon)^2}{d_{s,avg}^2 \varepsilon^3} \mu u + B' \frac{(1-\varepsilon)}{d_{s,avg} \varepsilon^3} \rho u^2 \tag{12}$$

$$\mathrm{Re}_{d_{s,avg}} = \frac{\rho u d_{s,avg}}{\mu} \tag{13}$$

In addition, the simulated results of the wet pressure drop were compared with the experimental results measured by our research group[15], as shown in Figure 4b. (The working conditions for this data are H_{CL} = 0.03 m, hydrophilic foam tray. The foam samples are of the same sort as Model B, the dimensions are L × W × H = 80 mm × 80 mm × 4 mm.) Through the comparison results of Figures 4a, b, it is found that the modeling and simulation method in this paper can accurately calculate the pressure drop of the foam tray based on the real structure.

4.3 The evolution of pressure drop and liquid holdup with bubble growth

Take the case of Model B, CA = 60°, U_g = 0.1 m/s, H_{CL} = 0.03 m as an example. Figure 5a is a schematic view of the main periods and stages of bubble formation at porous orifices. The color of the foam blocks in Figure 5a indicates the gas-liquid phase distribution of the internal pores, while the bubble boundary is selected as the interface

at a gas-phase volume fraction of 0.5. Figure 5b and Figure 5c show the evolution of the P_{total} and LHPC during the bubbling process. The colored marks in Figure 5b and the colored vertical lines in Figure 5c respectively represent the bubble characteristics at different stages of bubbling and correspond to Figure 5a.

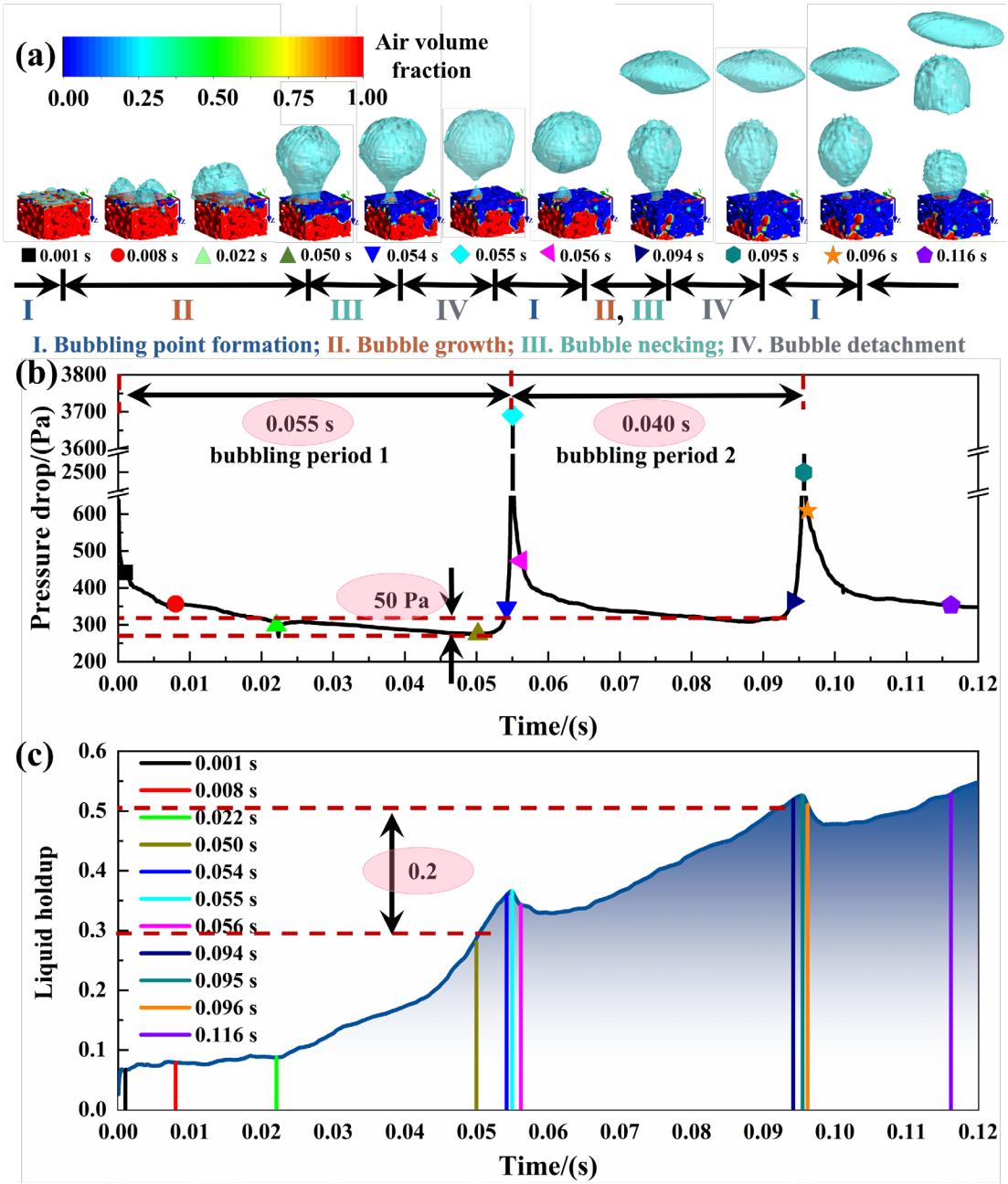

FIGURE 5 The bubbling behavior of the foam valve with Model B, when CA = 60°, U_g = 0.1 m/s and H_{CL} = 0.03 m; (a) Schematic view of the main periods and stages of bubble formation at porous orifice; (b) The evolution of P_{total} with flow time; (c) The evolution of LHPC with flow time.

First, we consider the time taken between two consecutive bubbles to completely detach from the foam tray as a bubbling period. And a bubbling period consists of four stages, which are bubble point formation (0 – 0.001 s), bubble growth (0.001 – 0.050 s), bubble necking (0.050 – 0.054 s) and bubble detachment (0.054 – 0.055 s), respectively. We can find that the variation laws of the P_{total} in these four stages are a rapid decrease, a slow decrease, a slow increase, and a rapid increase. And the bubble growth stage is the largest portion of the whole bubbling period. Comparing bubbling periods 1 and 2 in Figures 5b and c, we find that the bubbling period 2 is compared to 1. Its LHPC increased by 0.2, resulting in an increase of P_{total} by 50 Pa in the bubble growth stage, and the bubbling period was also shortened by 0.015 s. This also indicates the significant contribution of LHPC in the foam tray to P_{total} and foaming frequency. Moreover, the time for the bubbles to detached the foam tray corresponds to the peaks of P_{total} and LHPC in Figures 5b and c, whose frequencies further reflect the bubbling frequency within a fixed time period. Therefore, the subsequent chapters of this paper focus on the influence of operating conditions (superficial gas velocity (U_g) and clear liquid layer height (H_{CL})) and structural characteristics (foam structure (D_{pore} and ε) and wettability (CA)) on instantaneous LHPC and P_{total}.

4.4 The influence of superficial gas velocity on P_{total}

The U_g is one of the important factors that affect the P_{total} and LHPC. Figure 6a shows the schematic view of the leading bubble that is about to detach the foam tray under different U_g. The time corresponds to the color marks in Figures 6c, d. Figure 6b shows the mean P_{total} and the size of the D_{bubble} which can be calculated by Equation 14.

Figures 6c and d show the evolution of LHPC and P_{total} at different U_g.

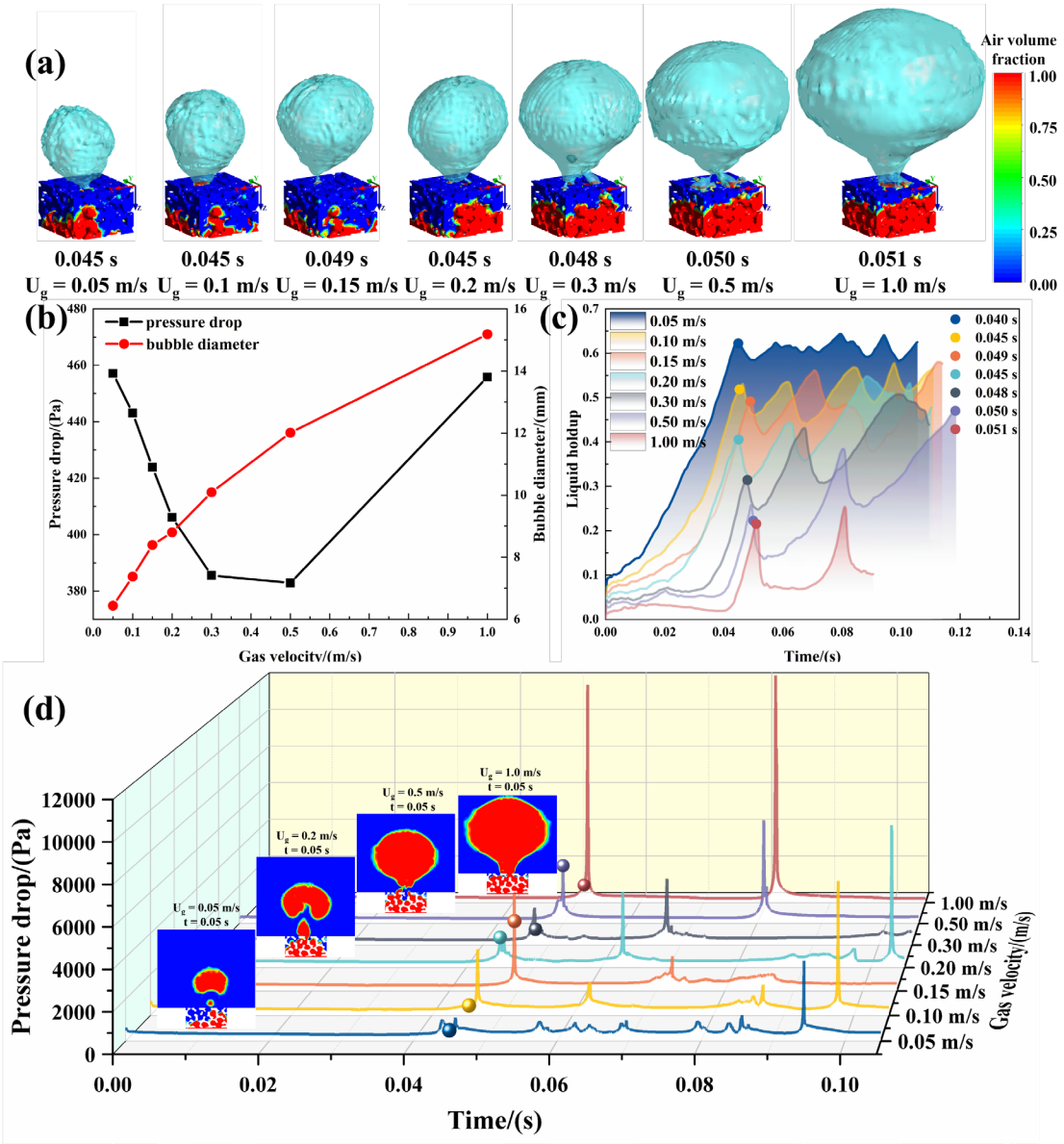

FIGURE 6 Operating conditions: Model B, CA = 45°, H_{CL} = 0.03m. (a) Schematic view of bubbles about to detach the orifice under different U_g;(b) The evolution of initial bubble diameter (D_{bubble}) and mean P_{total} with U_g;(c) The evolution of LHPC with flow time under different U_g; (d) The evolution of P_{total} with flow time under different U_g.

$$d_{bubble} = \left(\frac{6 \cdot V_{bubble}}{\pi} \right)^{1/3} \tag{14}$$

As shown in Figure 6b, the mean P_{total} first decreases and then increases with the increase of the U_g. The D_{bubble} increases with increasing U_g. From the discussion in the section 4.3, we know that the peak positions of P_{total} and LHPC correspond to the time

when the bubble leaves the foam tray. The peaks' frequency and height of P_{total} reflect the bubbling frequency and the dynamic pressure in the porous channels. In Figure 6d, When U_g = 0.05 m/s, the peak of P_{total} is high frequency and low value. As the U_g increases (0.1 m/s - 0.5 m/s), the peak frequency begins to downshift. With the U_g continues to increase (0.5m/s - 1.0m/s), the peak frequency hardly changes, but the peak value of P_{total} suddenly increases. Meanwhile, The LHPC has been decreasing with increasing U_g (in Figure 6c). When U_g = 0.05 m/s is compared with U_g = 0.5 m/s, the former LHPC is higher, resulting in a faster bubbling frequency and a higher mean P_{total}. When U_g = 0.5 m/s is compared with U_g = 1.0 m/s, the dynamic pressure in the foam pores of the latter is higher and the mean P_{total} is higher when the bubbling frequency is similar. This shows that LHPC is the key factor affecting the bubbling frequency of the foam tray, and the bubbling frequency and dynamic pressure are the key factors affecting the P_{total}.

4.5 The influence of wettability (static contact angle) on P_{total}

The wettability of the foam tray will affect the evolution of dynamic bubbles. For rigid surfaces, Young's equation (Equation 15) is a method to relate the interfacial tensions between each of the phase interfaces to the contact angle at the three-phase boundary. The detailed equation is as follows:

$$\sigma_{gl} \cdot \cos\theta_{wall} = \sigma_{sg} - \sigma_{sl} \tag{15}$$

where σ_{gl} is the surface tension at the gas-liquid interface, σ_{sg} is the surface tension at the solid/gas interface, and σ_{sl} is the surface tension at the solid/liquid interface.

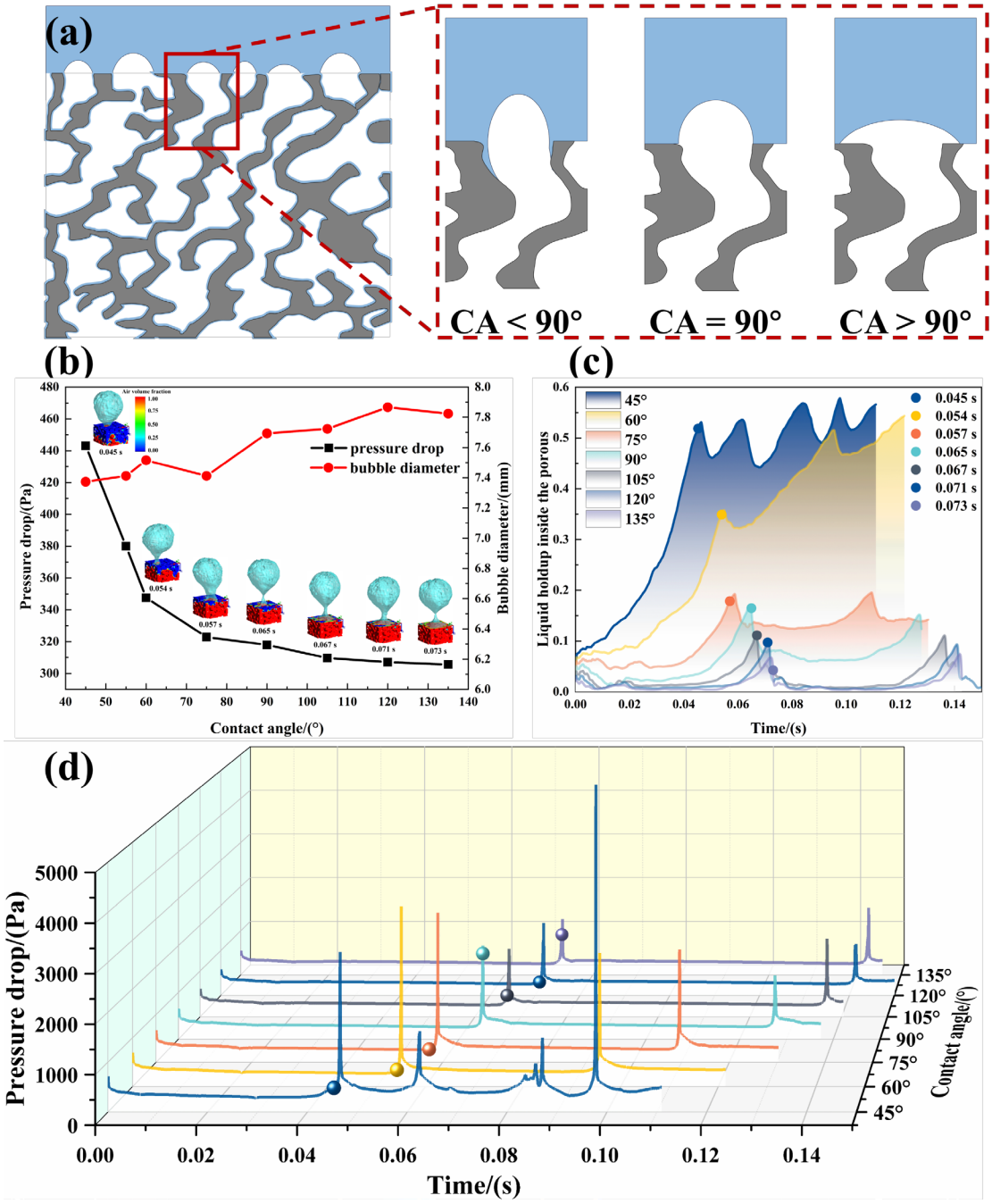

FIGURE 7 Operating conditions: Model B, U_g = 0.1 m/s, H_{CL} = 0.03 m. (a) Initial bubbling mechanism under different CA; (b) The evolution of D_{bubble} and mean P_{total} with CA; (c) The evolution of LHPC with flow time under different CA; (d) The evolution of P_{total} with flow time under different CA.

It can be known from Young's equation that the static contact angle (CA) will affect the energy difference between gas-solid and liquid-solid interaction. In Figure 7a, when CA < 90°, the energy of the liquid-solid interface will be smaller than that of the gas-

solid interface. Therefore, when the bubble grows to replace the liquid on the foam surface, kinetic energy must be applied to do work. In other words, the liquid attached to the foam surface is more likely to spontaneously replace the gas on the foam surface and cause the bubbles to detach the surface of the foam tray. When CA > 90^o , during the growth process of the bubble, the gas phase is easier to spontaneously replace the liquid on the foam surface, make it adhere to the foam surface and grow, and prolong the time for the bubble to detach the surface of the foam tray.

In Figure 7b, the mean P_{total} decreases and D_{bubble} increases with increasing CA. In Figure 7c, When CA increases, the LHPC becomes less and less until nothing. It can be seen from the peak position of the P_{total} (in Figure 8d) that the increasing CA decreased both the bubbling frequency and the dynamic pressure. This trend is also consistent with the trend of single submerged orifice[45]. Therefore, the following conclusions can be drawn: the increasing CA results in the enhancement of the liquid phase cohesion effect. Resulting in a decrease LHPC and dynamic pressure, an increase in the D_{bubble}, a decrease in bubbling frequency, and a decrease in the mean P_{total}.

4.6 The influence of clear liquid layer height on P_{total}

In this paper, different H_{CL} were established to further explore the contribution of LHPC to P_{total}. In Figure 8a, the SiC pressure drop (P_{SiC}) is the pressure drop difference in foam part. As the H_{CL} increases, the D_{bubble} becomes smaller, and the P_{total}, P_{SiC}, and LHPC increase. This is because the increased gravity of the liquid phase in the porous channel (Equation 11) leads to an increase in the LHPC, a decrease in the effective porosity of the foam tray, an increase in the dynamic pressure inside the channel, and

an increase in bubbling frequency, which ultimately increases the P_{SiC} and reduces the D_{bubble}. This further shows that the bubbling frequency, which is affected by the LHPC, is one of the key components in the P_{SiC}.

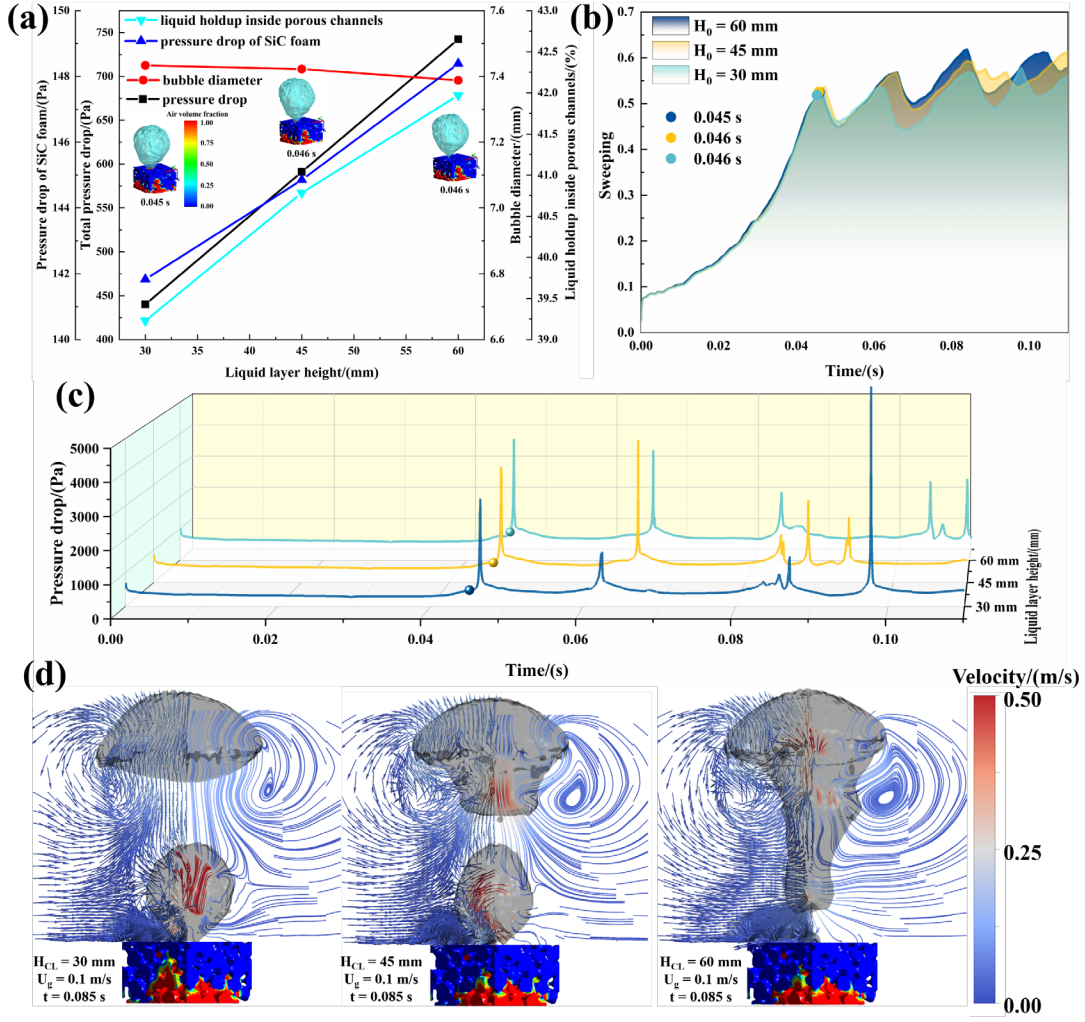

FIGURE 8 Operating conditions: Model B, CA = 45°, U_g = 0.1 m/s. (a) The evolution of D_{bubble}, P_{SiC}, P_{total} and LHPC with clear liquid layer height (H_{CL});(b) The evolution of LHPC with flow time under different H_{CL}; (c) The evolution of P_{total} with flow time under different H_{CL}; (d) Effects of H_{CL} on bubble flow pattern.

Moreover, due to the detached bubble that is farther from the water surface, the greater pressure on the bubble surface, the bubble is easily deformed to reduce the rising resistance. In Figure 8d, the higher the clear liquid layer height, the more likely the initial bubble detached the foam tray to coalesce and eventually form a large bubble

(Because the large bubble has greater lift and acceleration, which achieves a similar drag reduction effect [46]).

4.7 The influence of porous structure on P_{total}

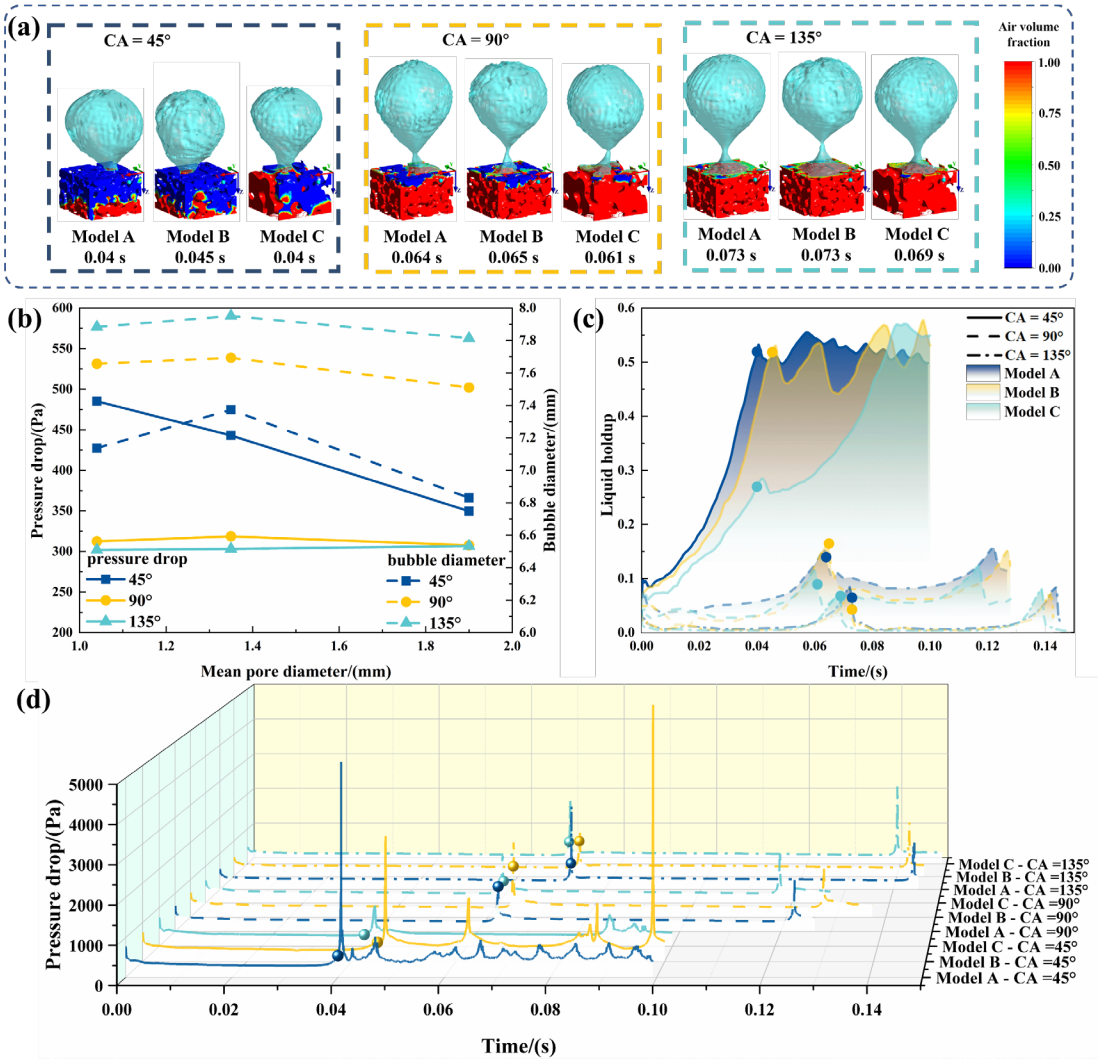

FIGURE 9 Operating conditions: H_{CL} = 0.03 m, U_g = 0.1 m/s. (a) Schematic view of bubbles about to leave the orifice under different porous structures;(b) The evolution of D_{bubble} and mean P_{total} with mean pore diameter (D_{pore});(c) The evolution of LHPC with flow time under different porous structures; (d) The evolution of P_{total} with flow time under different porous structures.

The detailed structural information of models A, B, and C is shown in Figure 1. As we all know, the most representative porous structure parameters are mean pore size and porosity. In Figure 9b, under different CA, model B with the largest porosity of 61.5% has the largest size of the D_{bubble}. This shows that the D_{bubble} is only related to the

porosity of the foam structure, not the mean pore size. When CA = 45°, model A with the smallest mean pore size has the largest P_{total}. Combining the peaks of LHPC and P_{total} in Figure 10c and Figure 10d, it can be concluded that the smaller the mean pore size, the more LHPC, the faster the bubbling frequency, resulting in larger P_{total}. However, when CA = 135°, the LHPC is almost 0 (Figures 10a, c). Model C with the smallest porosity has the fastest bubbling frequency and the largest P_{total}. This shows that the foam structure affects the P_{total} by affecting the LHPC and bubbling frequency.

5. New model of pressure drop for the foam tray

Through multi-factor investigation, it is concluded that the LHPC is the key component of the P_{total}. Therefore, the mean LHPC under the influence of various factors were calculated as shown in Figure 10a,b. In Figure 11a,b, when CA $\geq$ 90°, the LHPC is almost 0 during the bubbling process, which can be ignored. In addition, based on Yan's experimental results [16], it is also shown that when U_g > 1.3 m/s, there is no liquid weeping in the foam tray, which also shows that LHPC = 0. Therefore, with U_g = 1.3 m/s as the maximum superficial gas velocity, the equation of the LHPC is established (in Equation 16). The prediction results of Equation 16 is compared with the simulation results. It can be seen from Figure 10a, b that Equation 16 can well show the evolution of the LHPC with the foam structure (D_{pore}(mm)), the height of clear liquid layer (H_{CL}(m)), the static contact angle (CA(°)) and the superficial gas velocity (U_g(m/s)).

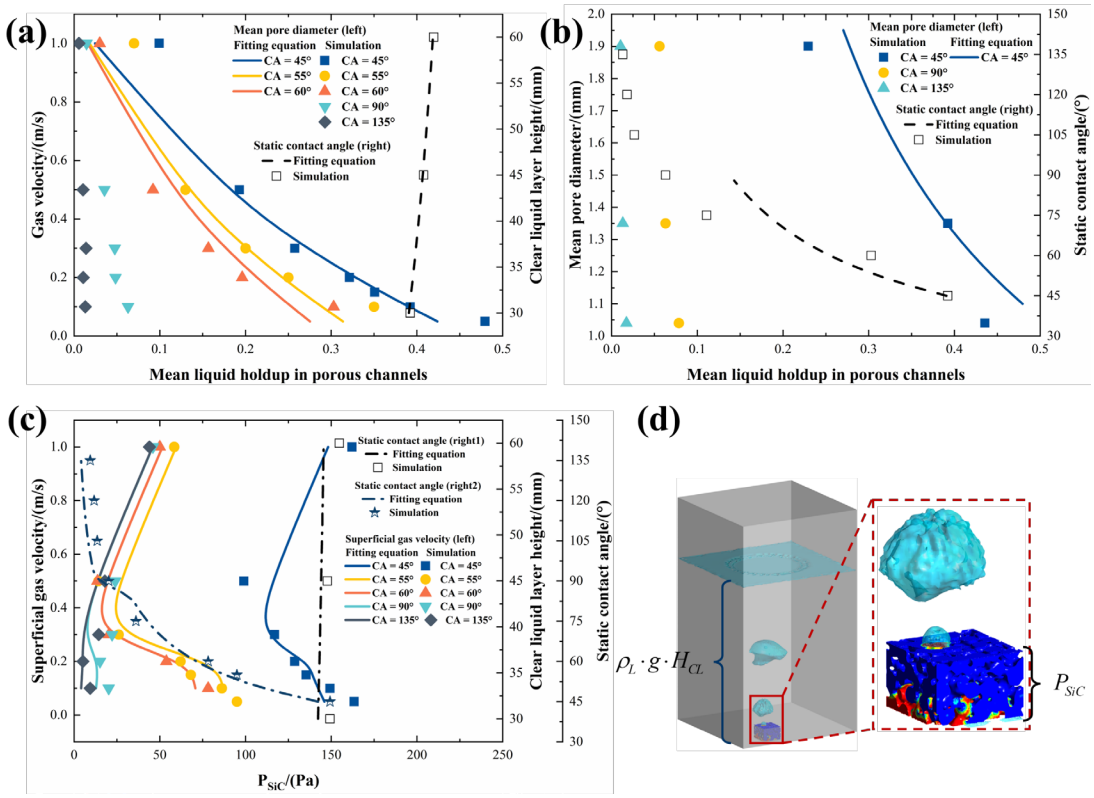

FIGURE 10 (a) The evolution of Ug and H_{CL} with mean LHPC; (b) The evolution of mean D_{pore} and wettability with mean LHPC; (c)The evolution of U_g, H_{CL} and CA with mean P_{SiC}; (d) Schematic diagram of pressure drop decomposition

$$\alpha_l = \begin{cases} 157 \cdot CA^{-1.5} \left(U_g - 1.3\right)^2 \cdot \mathrm{D}_{pore}^{-1} \cdot \mathrm{H}_{CL}^{0.1} & U_g < 1.3\,m/s \text{ and CA} < 90° \\ 0 & U_g \geq 1.3\,m/s \text{ or CA} \geq 90° \end{cases} \tag{16}$$

$$P_{total} = \rho_L \cdot g \cdot H_{CL} + P_{SiC} \tag{17}$$

$$P_{SiC} = P_{DRY} + P_{CA} \tag{18}$$

Pressure drop is one of the key factors in the application of foam trays. We decompose the P_{total} into a clear liquid head and P_{SiC} (in Figure 10d and Equation 17). The P_{SiC} is composed of the dry tray pressure drop (P_{dry}) and the CA-induced pressure drop (P_{CA}) (in Equation 18). The P_{CA} is the relationship between the U_g, CA, and LHPC. Based on experiments and simulations, the gas velocity at the lowest point of pressure drop (approximately 0.3 m/s) is analyzed. When U_g < 0.3 m/s, the contribution of the LHPC in the P_{CA} is greater, and when U_g > 0.3 m/s, the contribution of the U_g in the

P_{CA} becomes more and more significant. Based on this principle, Equation 20 for P_{CA} is proposed. The best constant in Equation 20 is obtained by the least-squares method as shown in Equation 21. It can also be seen from Equation 21 that when the U_g is low ($U_g < U_{cri}$) and the foam tray is hydrophilic (CA < 90°), the LHPC has a great influence on the P_{CA}. With the gas velocity increasing ($U_g > U_{cri}$), the P_{CA} is dominated by the dynamic pressure (U^2_g) in porous channels.

$$P_{DRY} = \left(A' \frac{(1-\varepsilon)^2}{d_{s,avg}^2 \varepsilon^3} \mu u + B' \frac{(1-\varepsilon)}{d_{s,avg} \varepsilon^3} \rho u^2 \right) \cdot L \tag{19}$$

$$P_{CA} = \begin{cases} C_0 \left(\frac{90}{CA} \right)^{C_1} + C_2 \cdot \alpha_l & U_g < 0.3 \\ C_0' \left(\frac{90}{CA} \right)^{C_1'} + C_2' \cdot \frac{U_g^2}{2} & U_g \geq 0.3 \end{cases} \tag{20}$$

$$P_{CA} = \begin{cases} 12 \cdot \left(\frac{90}{CA} \right)^3 + 117 \cdot \alpha_l & U_g < 0.3; 45° \leq CA \leq 135° \\ 0.1 \cdot \left(\frac{90}{CA} \right)^{10} + 20 \cdot U_g^2 & U_g \geq 0.3; 45° \leq CA \leq 135° \end{cases} \tag{21}$$

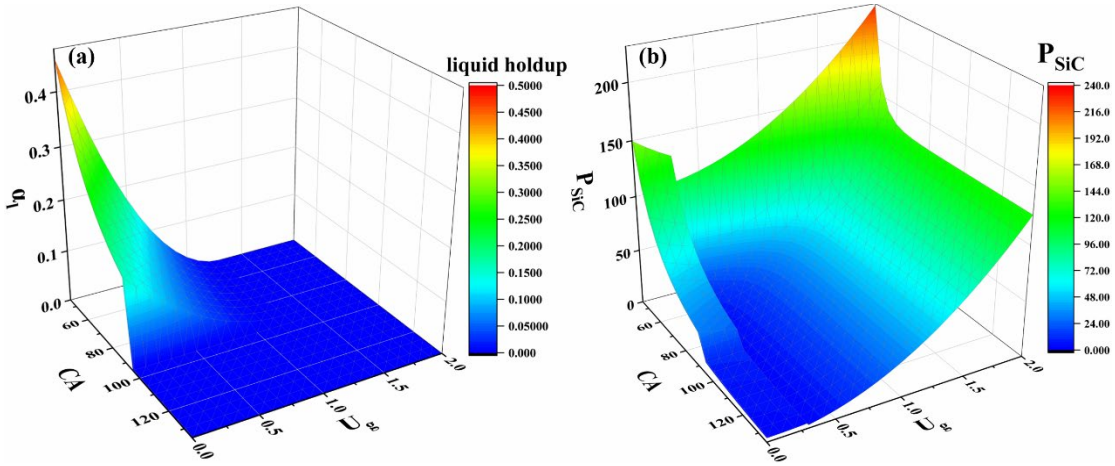

FIGURE 11 (a) Variations of LHPC with both U_g and CA;(b) Variations of P_{SiC} with both U_g and CA.

Taking Model B, H_{CL} = 0.03 m as an example, the variations of LHPC and P_{SIC} with both U_g and CA are shown in Figure 11. In Figure 11a, when U_g < 1.3 m/s and CA < 90° , The active porosity of the foam tray caused by LHPC must maintain smaller to

produce large enough force to overcome the resistance forces. However, the resistance force becomes smaller or driving force becomes larger with increasing CA or U_g, which is beneficial to open more gas channels, which means effective porosity becomes larger. In other words, increasing CA will reduce the resistance forces and contribute to decrease P_{SiC}, while increasing U_g will increase the driving forces and cause the P_{SiC} to decrease first and then increase. The first decrease in P_{SiC} is due to open more gas channels. If the effective channels have been fully utilized, the P_{SiC} will increase monotonically with increasing U_g. This also shows that for the purpose of reducing the P_{SiC}, the LHPC should be prevented from blocking the gas channels, to achieve the goal of reducing the P_{total}.

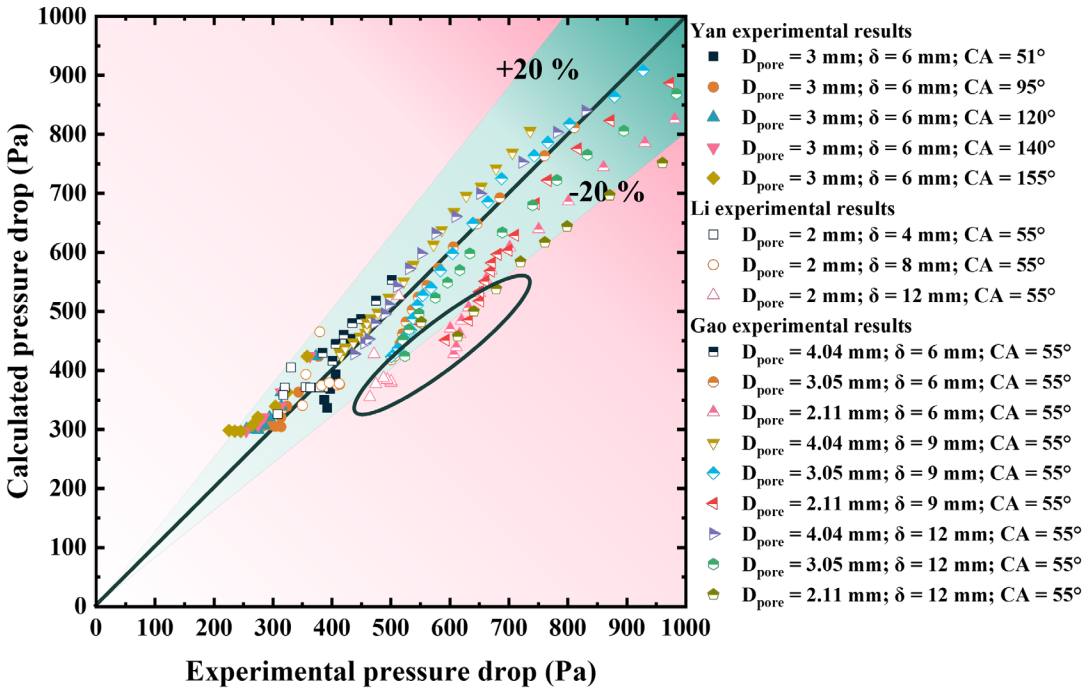

FIGURE 12 Comparison between Yan [16], Li [15] and Gao [47] experimental results of pressure drop on foam trays and the calculated values.

Based on the above results, the calculated value of the prediction model of the P_{total} (in Equation 19) was compared with the experimental value, as shown in Figure 12.

The deviations of most data are smaller than 20%. The predicted values of the model are in good consistency with the experimental values. Some of the calculated values are lower than the experimental values (The region enclosed by the blue ellipse in Figure 12). The main reason is that when the thickness of the foam tray increases to 12 mm, the LHFP in the predicted model is underestimated, resulting in the predicted total pressure drop lower than the actual situation. To sum up, this model will be effective for the prediction of total pressure drop of the foam tray.

6. Conclusion

Based on the tomographic reconstruction of the real foam structure and using this as a geometric model. The effects of U_g, CA, H_{CL}, and foam structure (Model A, Model B, and Model C) on the LHPC, dynamic bubbling process, and P_{total} are investigated, and the following conclusions were obtained.

During the dynamic bubbling process with the foam tray as the orifice, the P_{SiC} is mainly composed of the bubbling frequency (pressure drop peak) and the dynamic pressure in the porous channels (with bubble growth, the pressure drop converted by the gas phase kinetic energy of the internal porous channels). Foam trays with complex struts tend to hold LHPC and block the gas channels, which makes the bubbling frequency faster and causes abnormally high pressure. Increasing the CA, U_g, porosity, and mean pore diameter can effectively reduce the LHPC. To make it satisfy one of extending the bubbling frequency or reducing the dynamic pressure in the porous channels to achieve the purpose of reducing the P_{total}. Therefore, this paper builds a new pressure drop correlation equation under based on the LHPC caused by the influence

of multiple factors. This model has good predictability and provides a valuable reference for the application and development of foam trays.

Acknowledgments

The authors are grateful for the financial support from the National Natural Science Foundation of China (No. 22178249) and Haihe Laboratory of Sustainable Chemical Transformations.

Nomenclature

α_i	the volume fraction of the i phase, dimensionless
ε	porosity
F_{VOL}	volume force, **N**
R	radius, **m**
g	gravitational acceleration, **m/s^2**
P	system pressure, **MPa**
Re	Reynolds number
U_g	superficial gas velocity at gas inlet, **m/s**
U_{cri}	Critical superficial gas velocity at gas inlet, **m/s**
μ	viscosity, **mPa·s**
σ	surface tension, **N/m**
t	flow time, **s**
ρ	density, **kg/m^3**
CA	static contact angle,^{o}
P_{CA}	CA-induced pressure drop, **Pa**

P_{DRY}	dry tray pressure drop, **Pa**
P_{SiC}	SiC foam pressure drop, **Pa**
P_{total}	Total pressure drop, **Pa**
L	SiC foam thickness, **m**
H_{CL}	clear liquid layer height, **m**
D_{pore}	SiC foam pore size, **mm**
D_{bubble}	initial bubble size, **mm**

Abbreviations

CFD	computational fluid dynamics
CSF	continuous surface force
LHPC	Liquid holdup in porous channels

Subscripts

g	gas phase
l	liquid phase

References

1. Hemmat Esfe M, Bahiraei M, Hajbarati H, Valadkhani M. A comprehensive review on convective heat transfer of nanofluids in porous media: Energy-related and thermohydraulic characteristics. *Applied Thermal Engineering*. 2020;178

2. Niu Z, Pinfield VJ, Wu B, et al. Towards the digitalisation of porous energy materials: evolution of digital approaches for microstructural design. *Energy & Environmental Science*. 2021;14(5):2549-2576.

3. Wood BD, He X, Apte SV. Modeling Turbulent Flows in Porous Media. *Annual Review of Fluid Mechanics*. 2020;52(1):171-203.

4. Zhang L, Liu X, Li H, et al. Hydrodynamic and Mass Transfer Performances of a New SiC Foam Column Tray. *Chemical Engineering & Technology*. 2012;35(12):2075-2083.

5. Zhang L, Liu X, Li X, et al. A Novel SiC Foam Valve Tray for Distillation Columns. *Chinese Journal of Chemical Engineering*. 2013;21(8):821-826.

6. Gao X, Yan P, Ma X, Zhao Z, Li H, Li X. Design of distillation reactor with novel catalysts distribution pattern for n-amyl acetate synthesis in industrial scale. *Fuel*. 2020;280

7. Li H, Shi Q, Yang X, Li X, Gao X. Characterization of Novel Carbon Foam Corrugated Structured Packings with Varied Corrugation Angle. *Chemical Engineering & Technology*. 2018;41(1):182-191.

8. Li H, Wang F, Wang C, Gao X, Li X. Liquid flow behavior study in SiC foam corrugated sheet using a novel ultraviolet fluorescence technique coupled with CFD simulation. *Chemical Engineering Science*. 2015;123:341-349.

9. Li X, Gao G, Zhang L, et al. Multiscale Simulation and Experimental Study of Novel SiC Structured Packings. *Industrial & Engineering Chemistry Research*. 2012;51(2):915-924.

10. Gao X, Ding Q, Wu Y, et al. Kinetic study of esterification over structured ZSM-5-coated catalysts based on fluid flow situations in macrocellular foam materials. *Reaction Chemistry & Engineering*. 2020;5(3):485-494.

11. Masson R, Keller V, Keller N. β-SiC alveolar foams as a structured photocatalytic support for the gas phase photocatalytic degradation of methylethylketone. *Applied Catalysis B: Environmental*. 2015;170-171:301-311.

12. Ou X, Pilitsis F, Jiao Y, et al. Hierarchical Fe-ZSM-5/SiC foam catalyst as the foam bed catalytic reactor (FBCR) for catalytic wet peroxide oxidation (CWPO). *Chemical Engineering Journal*. 2019;362:53-62.

13. Ou X, Xu S, Warnett JM, et al. Creating hierarchies promptly: Microwave-accelerated synthesis of ZSM-5 zeolites on macrocellular silicon carbide (SiC) foams. *Chemical Engineering Journal*. 2017;312:1-9.

14. Lévêque J, Rouzineau D, Prévost M, Meyer M. Hydrodynamic and mass transfer efficiency of ceramic foam packing applied to distillation. *Chemical Engineering Science*. 2009;64(11):2607-2616.

15. Li H, Fu L, Li X, Gao X. Mechanism and analytical models for the gas distribution on the SiC foam monolithic tray. *AIChE Journal*. 2015;61(12):4509-4516.

16. Yan P, Li X, Li H, Gao X. Hydrodynamics and flow mechanism of foam column Trays: Contact angle effect. *Chemical Engineering Science*. 2018;176:220-232.

17. Yan P, Li X, Li H, Shao Y, Zhang H, Gao X. Hydrodynamics and mechanism of hydrophobic foam column tray: Contact angle hysteresis effect. *AIChE Journal*. 2019;66(1)

18. Wallenstein M, Hafen N, Heinzmann H, et al. Qualitative and quantitative insights into multiphase flow in ceramic sponges using X-ray computed tomography. *Chemical Engineering Science*. 2015;138:118-127.

19. Gunjal PR, Kashid MN, Ranade VV, Chaudhari RV. Hydrodynamics of Trickle-Bed Reactors: Experiments and CFD Modeling. *Industrial & Engineering Chemistry Research*. 2005;44(16):16.

20. Li X, Yan P, Zhao S, Li H, Gao X. Fabrication and hydrodynamics performance of modified sieve tray with Janus feature. *Separation and Purification Technology*. 2019;216:74-82.

21. G. Fourie J, P. Du Plessis J. Pressure drop modelling in cellular metallic foams. *Chemical Engineering Science*. 2002;57(14):2781-2789.

22. Habisreuther P, Djordjevic N, Zarzalis N. Statistical distribution of residence time and tortuosity of flow through open-cell foams. *Chemical Engineering Science*. 2009;64(23):4943-4954.

23. Kumar P, Topin F. Investigation of fluid flow properties in open cell foams: Darcy and weak inertia regimes. *Chemical Engineering Science*. 2014;116:793-805.

24. Rambabu S, Kartik Sriram K, Chamarthy S, Parthasarathy P, Ratna kishore V. A proposal for a correlation to calculate pressure drop in reticulated porous media with the help of numerical investigation of pressure drop in ideal & randomized reticulated structures. *Chemical Engineering Science*. 2021;237

25. Hutter C, Zenklusen A, Kuhn S, Rudolf von Rohr P. Large eddy simulation of flow through a streamwise-periodic structure. *Chemical Engineering Science*. 2011;66(3):519-529.

26. Jorge P, Mendes MAA, Werzner E, Pereira JMC. Characterization of laminar flow in periodic open-cell porous structures. *Chemical Engineering Science*. 2019;201:397-

412.

27. Nie Z, Lin Y, Tong Q. Numerical simulations of two-phase flow in open-cell metal foams with application to aero-engine separators. Article. *International Journal of Heat and Mass Transfer*. 2018;127:917-932.

28. Zenklusen A, Kenjereš S, Rohr PRv. Mixing at high Schmidt number in a complex porous structure. *Chemical Engineering Science*. 2016;150:74-84.

29. Zenklusen A, Kenjereš S, Rudolf von Rohr P. Vortex shedding in a highly porous structure. *Chemical Engineering Science*. 2014;106:253-263.

30. Blazejczyk A. Morphometric analysis of one-component polyurethane foams applicable in the building sector via X-ray computed microtomography. Article. *Mater*. 2018;11(9)1717.

31. Chen Y, Das R, Battley M. An approach for characterising cellular polymeric foam structures using computed tomography. In: *AIP Conference Proceedings*. American Institute of Physics Inc.; 2018: 020002.

32. De Carvalho TP, Morvan HP, Hargreaves D, Oun H, Kennedy A. Experimental and tomography-based CFD investigations of the flow in open cell metal foams with application to aero engine separators. In: *Proceedings of the ASME Turbo Expo*. American Society of Mechanical Engineers (ASME); 2015: V05CT15A028.

33. Ou X, Zhang X, Lowe T, et al. X-ray micro computed tomography characterization of cellular SiC foams for their applications in chemical engineering. *Materials Characterization*.2017;123:20-28.

34. Fan X, Ou X, Xing F, et al. Microtomography-based numerical simulations of heat

transfer and fluid flow through β -SiC open-cell foams for catalysis. *Catalysis Today*. 2016;278:350-360.

35. Torre AD, Montenegro G, Onorati A, Tabor G. CFD Characterization of Pressure Drop and Heat Transfer Inside Porous Substrates. *Energy Procedia*. 2015;81:836-845.

36. Yu P, Wang Y, Ji R, Wang H, Bai J. Pore-scale numerical study of flow characteristics in anisotropic metal foam with actual skeleton structure. *International Communications in Heat and Mass Transfer*. 2021;126:105401.

37. George GR, Bockelmann M, Schmalhorst L, et al. Workflow for computational fluid dynamics modeling of fixed‐bed reactors packed with metal foam pellets: Hydrodynamics. *AIChE Journal*. 2021:e17284.

38. Bracconi M, Ambrosetti M, Okafor O, et al. Investigation of pressure drop in 3D replicated open-cell foams: Coupling CFD with experimental data on additively manufactured foams. *Chemical Engineering Journal*. 2019;377:120123.

39. Sun M, Hu C, Zha L, et al. Pore-scale simulation of forced convection heat transfer under turbulent conditions in open-cell metal foam. *Chemical Engineering Journal*. 2020;389:124427.

40. Reay D. Metal Foams: Fundamentals and Applications. *Applied Thermal Engineering*. 2013;61(2)

41. Meinicke S, Möller C-O, Dietrich B, Schlüter M, Wetzel T. Experimental and numerical investigation of single-phase hydrodynamics in glass sponges by means of combined μPIV measurements and CFD simulation. *Chemical Engineering Science*. 2017;160:131-143.

42. Della Torre A, Montenegro G, Tabor GR, Wears ML. CFD characterization of flow regimes inside open cell foam substrates. *International Journal of Heat and Fluid Flow*. 2014;50:72-82.

43. Li H, Yi F, Li X, Gao X. Numerical modeling of mass transfer processes coupling with reaction for the design of the ozone oxidation treatment of wastewater. *Frontiers of Chemical Science and Engineering*. 2021, 15(3): 602-614.

44. Brackbill JU, Kothe DB, Zemach C. A continuum method for modeling surface tension. *Jcompphys*. 1992;100(2):335-354.

45. Hecht KJ, Velagala S, Easo DA, Saleem MA, Krause U. Influence of Wettability on Bubble Formation from Submerged Orifices. *Industrial & Engineering Chemistry Research*. 2019;59(9):4071-4078.

46. Verschoof RA, van der Veen RC, Sun C, Lohse D. Bubble Drag Reduction Requires Large Bubbles. *Phys Rev Lett*. Sep 2 2016;117(10):104502.

47. Gao X, Li X, Liu X, Li H, Yang Z, Zhang J. A novel potential application of SiC ceramic foam material to distillation: foam monolithic tray. *Chemical Engineering Science*. 2015;135:489-500.